

Vortex shedding induced vibration of thin strip in confined rectangular channel

Botao Zhang^a, Shengjie Gong^{a,*}, Shichang Dong^a, Zhenqin Xiong^a, Zhen Zhang^b

^a School of Nuclear Science and Engineering, Shanghai Jiao Tong University, Shanghai, China

^b CNNC Key Laboratory on Nuclear Reactor Thermal Hydraulics Technology, Nuclear Power Institute of China, Sichuan, China



ARTICLE INFO

Keywords:
Elongated plates
Vortex shedding
Sidewall effect

ABSTRACT

To study the basic behavior of vortex shedding of spacer grids, both experiments and numerical simulations of a single flat plate with a high chord-to-thickness ratio in a confined rectangular channel were performed. Frequencies of vortex-induced vibrations were obtained through a laser Doppler vibrometer (LDV), and the upstream velocity distribution was acquired by particle image velocimetry (PIV). Two-dimensional large eddy simulations (LES) were conducted, with the PIV results being used as the inlet boundary conditions. Dynamic mode decomposition (DMD) was applied to the numerical results to identify the vortex shedding modes for a number of cases. The numerical results showed good agreement with the experiments in terms of the vortex shedding frequencies. From the simulations, three vortex shedding modes were obtained: trailing edge shedding without the leading edge–vortices coupling (Type I), weak leading edge–vortices coupled shedding (Type II), and strong leading edge–vortices coupled shedding (Type III). The leading edge vortices showed different types of characteristics, namely those that diffused before reaching the trailing edge (Type I), those that stayed close to the plate surface until they reached the trailing edge (Type II), and those that got detached from the plate surface in the transverse direction, and then moved back (Type III). The results showed that both the Reynolds number based on the plate thickness (Re_d) and dimensionless width of the channel (h/d) could affect the vortex shedding. A higher Re_d or lower h/d led to stronger leading edge vortices. Moreover, stronger leading edge vortices led to a smaller dimensionless boundary layer thickness (δ/d) at the trailing edge. Finally, the Strouhal number based on the separation distances between similarly shed rotational vortices (St_s) and the thickness of the plate together with the boundary layer ($St_{d+2\delta}$) were more robust than that based on the thickness of the plate (St_d).

1. Introduction

Safety is a critical issue for nuclear power plants right from their design to operation. In addition to safety, performance and economy are also affected by component failures in reactors. Generally, such failures are caused by excessive vibrations caused by fluid flow (Pettigrew et al., 1998). For rod-to-grid type fuel assemblies, which are widely used in most pressurized water reactors (PWRs), flow-induced vibrations can lead to grid-to-rod fretting (GTRF). The fretting wear may cause fuel rod failures, which result in the leakage of radioactive substances and threaten the safety of the plant. Kim (2009) and Jiang et al. (2016) numerically studied the fretting wear of PWR fuel assemblies. To evaluate the GTRF behavior, the dynamic characteristics of flow-induced vibrations of the nuclear fuel assembly needs to be obtained. For example, the vibrations induced by turbulent axial flows around bare

rod bundles were investigated by De Santis et al. (2018) by employing fluid–structure coupled simulations. In the past few decades, flow-induced vibrations of a single rod or rod bundles have been widely studied compared to spacer grids; moreover, the vibrations have been mostly investigated in the low-frequency domain. However, Zhang et al. (2017) reported high-frequency vibrations at a spacer grid with considerable amplitudes. Such high-frequency vibrations could cause a frequent grid-to-rod contact and accelerate the failure process. Thus, it is necessary to study the flow-induced vibration characteristics of spacer grids. The flow-induced vibrations can be caused by three phenomena, namely turbulence excitation, vortex shedding, and fluid-elastic instability (Kaneko et al., 2014; Weaver et al., 2000). Unlike the fuel rods in axial flows, spacer grids suffer from cross flow while the power plants are in operation. Therefore, vortex shedding would be the main source of excitation for spacer grids. Despite the complex geometry of spacer

* Corresponding author.

E-mail address: gsj@sjtu.edu.cn (S. Gong).

grids, this problem can be simply formulated in terms of a thin strip subjected to a cross flow in a narrow channel.

Vortex shedding of plates has been widely investigated in the past because they are basic important structures in various disciplines, such as ocean engineering, wind engineering, and aerodynamics. Parker (1966) studied wake shedding from a single plate and parallel plates by acquiring sound pressure trace using a microphone. In the early years, experiments on vortex shedding by rectangular flat plates were performed in a wind tunnel. Pressure sensors, hot wires, and microphones were employed to measure the fluctuations in the fluid flow, and the smoke wire method was also used to visualize flow the fields (Nakamura et al., 1991; Parker and Welsh, 1983; Shiraishi and Matsumoto, 1983; Welsh and Gibson, 1979). After analyzing the results obtained by Parker and Welsh (1983), Stokes and Welsh (1986) summarized the vortex shedding regimes of a flat plate with square leading and trailing edges in an open space. The experiments were conducted under a high Reynolds number based on the thickness of the plate ($Re_d \geq 14,800$). Various regimes were obtained based on the chord-to-thickness ratio (c/d) as follows:

- (a) On short plates ($c/d < 3.2$), flow separation occurred at the leading edge corner without being reattached to the plate surface, and a regular vortex street was formed in the wake region.
- (b) On long plates ($3.2 \leq c/d \leq 7.6$), the shear layers got reattached to the trailing edge surface periodically. The separation bubble grew, enveloping the trailing edge.
- (c) On longer plates ($7.6 < c/d \leq 16$), the shear layers were always reattached upstream of the trailing edge and formed a separation bubble, which grew, and was divided in a random manner. No regular vortex shedding was observed.
- (d) For plates with $c/d > 16$, the shear layers were reattached; however, they diffused before reaching the trailing edge. The characteristics of the boundary layers on either side of the plate approached a fully developed turbulent state, and interacted to form a regular vortex street that is not directly related to the formation of the leading-edge separation bubbles.

Nakamura et al. (1991) found that regular vortex shedding appeared in regime (c) when $Re_d < 2000$, and the regular vortex street disappeared for $12 < c/d < 15$ when $Re_d > 2000$. After introducing perturbations by applying sound, Parker and Welsh (1983) found that regular vortex shedding appeared again under high values of Re_d , and the vortex shedding frequency could be locked to the applied sound frequency over a wide range. Moreover, Mills et al. (2002) found that trailing edge shedding could lock the leading edge shedding, and the strongest shedding mode occurred when the applied sound frequency matched the preferred natural shedding. Welsh and Gibson (1979) performed experiments on flow past a square leading-edge plate in a duct and found that vortex shedding could be excited into a β -mode resonance. In addition, shape of the cross section (Hourigan et al., 2001; Naghib-Lahouti et al., 2014; Naudascher and Wang, 1993; Parker and Welsh, 1983; Shiraishi and Matsumoto, 1983; Taylor et al., 2011), incident vortex street (Zhang and Liu, 2015), incidence (Rojratsirikul et al., 2011), and transverse forcing (Tan et al., 2004) could also affect the shedding behavior.

However, time-averaged properties and instantaneous information are not adequate for analyzing the flow structures. Therefore, modal decomposition techniques such as proper orthogonal decomposition (POD) and dynamic mode decomposition (DMD) are employed to analyze the vortex shedding modes of a flat plate. DMD can provide the dynamic characteristics of the flow fields and has been successfully applied in many studies (Kou et al., 2018; Rowley et al., 2009; Schmid, 2010; Tu et al., 2014). Shi et al. (2010) employed particle image velocimetry (PIV) to measure separated flow over a blunt plate, and large-scale vortices in the separated shear layer for different values of c/d were identified by applying POD. Moreover, Liu and Zhang (2015)

used DMD to identify the shedding mode for blunt plates with $c/d = 3, 6$, and 9. For $c/d = 6$ and 9, the leading edge and trailing edge shedding modes were obtained from the PIV measurements in a water tunnel.

Mondal et al. (2020) numerically investigated the effect of sidewalls for prisms with $c/d = 3$ under laminar flow conditions. Different vortex shedding modes were identified by varying the distance between the prisms. The vortex shedding frequency increased with decreasing gap size, implying that the sidewalls had a strong influence on the vortex shedding. However, few investigations have been performed on the effect of sidewalls on the vortex shedding characteristics of elongated plates.

For the spacer grid, where c/d is significantly large and the space is quite small, different vortex shedding behaviors can be observed. A large c/d would result in a leading edge vortex shedding, and a small space would accelerate the vortex shedding, and both of them could affect the shedding frequency. Strong resonance caused by vortex shedding should be avoided for the spacer grid to prevent fuel rod failure, and the shedding frequency, which is intimately related to vortex shedding behavior, is a key parameter. Therefore, in the present study, both experiments and numerical simulations were employed to investigate the vortex shedding characteristics of elongated plates in a confined rectangular channel. The flow-induced vibration spectra of the plates were measured using a laser Doppler vibrometer (LDV) system, and the time-averaged velocity profile upstream of the plate was obtained from a PIV system. In addition, two-dimensional large eddy simulations (LES) were adopted to acquire detailed information on the flow fields, and the DMD proposed by Schmid (2010) was used to identify the vortex shedding modes. Based on the combination of experimental and numerical results, both qualitative and quantitative analyses were conducted.

2. Methods

2.1. Experimental method

Experiments were carried out in a closed-circuit setup at ambient temperature (20 °C) and atmospheric pressure (0.1 MPa). Deionized water was driven by a centrifugal pump and flowed through the test section with a bulk velocity (U_b) of 2 m/s. The test section was a 2000-mm long transparent narrow channel made of acrylic with a 12×66 mm² rectangular cross-section. A flat plate, made of stainless steel, was fixed at the center of the channel by clamping the two opposite sides. Both the leading and trailing edges of the plate were square, and the leading edge was 1000 mm away from the entrance of the test section. The experimental setup is shown in Fig. 1(a) and (b). Five different plates were used in the present study with thickness (d) of 0.30, 0.52, 0.92, 1.39, and 1.92 mm, and chord (c) of 16.8 mm.

An LDV system (non-contact measurement technique) was used to measure the vibration velocity of the thin plate, as shown in Fig. 1(a). It had a measurement range of ± 50 mm/s and a resolution of 0.1 μm/s; the measurement linear error was 1%. A laser emitted by the LDV system, would pass through the transparent wall of the water channel, then get reflected by a stainless-steel plate, and collected by a receiver. Then, the vibration velocity in the transverse direction was acquired by analyzing and processing the frequency shift of the laser signal. The sampling frequency was set to 10 kHz. The LDV was supported and regulated by a tripod with an adjustment knob. In addition, an optical table was used to fix the tripod and isolate the vibration disturbance from the ambient environment. For each test, the vibration data were acquired when the flow reached a steady state. The data were transformed by applying a fast Fourier transform (FFT) and Hanning window, and each sequence contained 10,000 points, which led to a resolution of 1 Hz. Finally, the averaged results of the specified tests were obtained by processing the continuous sequences.

The velocity profile along the transverse direction (same as the direction of the vibration velocity) before the thin plate was measured by a 2D PIV system, which contained a pulse laser, CCD camera, controlling

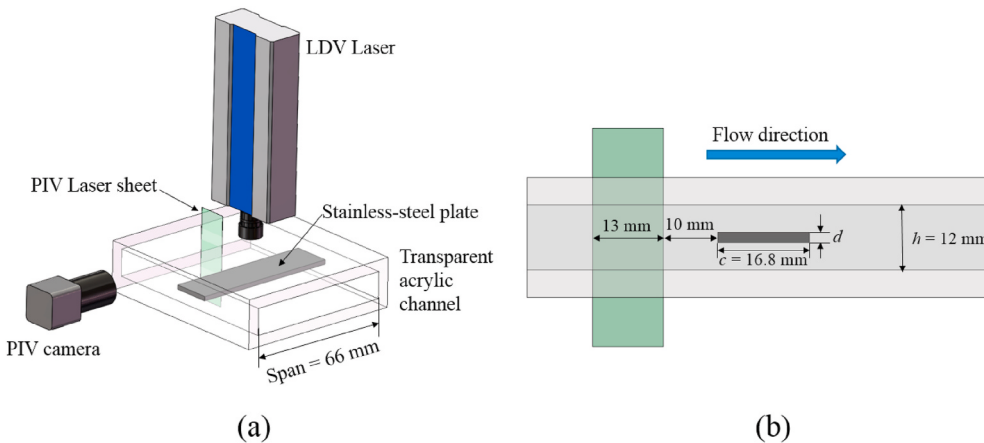


Fig. 1. Schematic of the experimental setup: (a) overview of the experimental facility and (b) mid-plane and dimensions.

device, and cooling system. The data recording frequency was 10 Hz, and 30 snapshots were acquired to calculate the time-averaged velocity profile. The PIV region was a rectangle ($13 \times 12 \text{ mm}^2$), whose top boundary was 10 mm upstream of the leading edge of the plate.

2.2. Numerical method

To validate the effectiveness of the CFD model in simulating the flow around a long flat plate in a confined space, numerical simulations were carried out. Large eddy simulation (LES) was employed in the present study to numerically investigate the flow fields around the plate, as direct numerical simulation (DNS) would require expensive computing resources, and the Reynolds-averaged Navier-Stokes (RANS) models cannot adequately provide unsteady flow information. In LES, each field variable φ can be decomposed into a filtered part $\overline{\varphi}$ and a residual part φ' :

$$\varphi = \bar{\varphi} + \varphi' \quad (1)$$

The filtered variable is defined as

$$\bar{\varphi} = \int \varphi(x') G(x, x') dx' \quad (2)$$

where G is the filter function that determines the scale of the resolved eddies.

The governing equations of the LES adopted in this study were obtained by filtering the time-dependent Navier-Stokes equations. For incompressible flows, the filtered continuity and momentum equations are:

$$\frac{\partial u_i}{\partial x_j} = 0 \quad (3)$$

$$\frac{\partial \bar{u}_i}{\partial t} + \frac{\partial (\bar{u}_i \bar{u}_j)}{\partial x_i} = \frac{\mu}{\rho} \frac{\partial^2 \bar{u}_i}{\partial x_j \partial x_j} - \frac{1}{\rho} \frac{\partial \bar{p}}{\partial x_i} - \frac{\partial \tau_{ij}}{\partial x_j} \quad (4)$$

where \bar{u}_i , x_i , \bar{p} , μ , ρ , and t are the velocity component, coordinate component, pressure, dynamic viscosity, density, and time, respectively. τ_{ij} is the subgrid-scale stress, defined as

$$\tau_{ij} = \overline{u_i u_j} - \bar{u}_i \bar{u}_j \quad (5)$$

The subgrid-scale stress needs to be modeled, for which a commonly used approach involves applying the Boussinesq hypothesis, which computes the stress tensor as follows:

$$\tau_{ij} - \frac{1}{3}\tau_{kk}\delta_{ij} = -2\mu_t \overline{S}_{ij} \quad (6)$$

where μ_t is the subgrid-scale turbulent viscosity, and $\overline{S_{ij}}$ is the resolved strain rate defined as

$$\overline{S_{ij}} = \frac{1}{2} \left(\frac{\partial \overline{u}_i}{\partial x_j} + \frac{\partial \overline{u}_j}{\partial x_i} \right) \quad (7)$$

In this study, the subgrid-scale turbulent viscosity μ_t was resolved by the wall-adapting local eddy viscosity (WALE) model (Nicoud and Ducros, 1999), given as follows:

$$\mu_t = (C_w \Delta)^2 \frac{\left(S_{ij}^d S_{ij}^d \right)^{3/2}}{\left(\overline{S}_{ij} S_{ij} \right)^{5/2}} + \left(S_{ij}^d S_{ij}^d \right)^{5/4} \quad (8)$$

where S_{ij}^d is the traceless symmetric tensor of the square of the velocity gradient tensor.

$$S_{ij}^d = \frac{1}{2} \left(\frac{\partial \bar{u}_i}{\partial x_k} \frac{\partial \bar{u}_k}{\partial x_j} + \frac{\partial \bar{u}_j}{\partial x_k} \frac{\partial \bar{u}_k}{\partial x_i} \right) - \frac{1}{3} \delta_{ij} \frac{\partial \bar{u}_k}{\partial x_k} \frac{\partial \bar{u}_k}{\partial x_k} \quad (9)$$

The coefficient C_w was set to 0.325. With this spatial operator, the WALE model is designed to return the correct wall asymptotic behavior for wall-bounded flows.

Considering that the span of the plate was significantly larger than the thickness and chord, the two-dimensional model was adopted in this study. The dimensions used in various numerical cases investigated are summarized in [Table 1](#). Both experimental and numerical investigations were conducted for Cases 1–5, while only numerical investigations were conducted for Case 6. The computational domain is shown in [Fig. 2\(a\)](#) and consisted of four parts, namely inlet, outlet, wall, and plate. The inlet was 10 mm from the leading edge of the plate, and the outlet was located at $2c$ far from the trailing edge. The distance between the upper and lower walls was h (12 mm for the experiments), and the chord of the plate was d . The mesh generation is shown in [Fig. 2\(b\)](#), and the y^+ was approximately 1.

The inlet was set to “Velocity Inlet” and the time-averaged velocity

Table 1
Parameters for different simulation cases.

Case ID	d/mm	c/d	h/d	Re_d	Experiment
Case 1	0.30	56.0	40	597	●
Case 2	0.52	32.3	23.1	1035	●
Case 3	0.92	18.3	13.0	1831	●
Case 4	1.39	12.1	8.6	2767	●
Case 5	1.92	8.8	6.3	3822	●
Case 6	1.92	56.0	40	3822	○

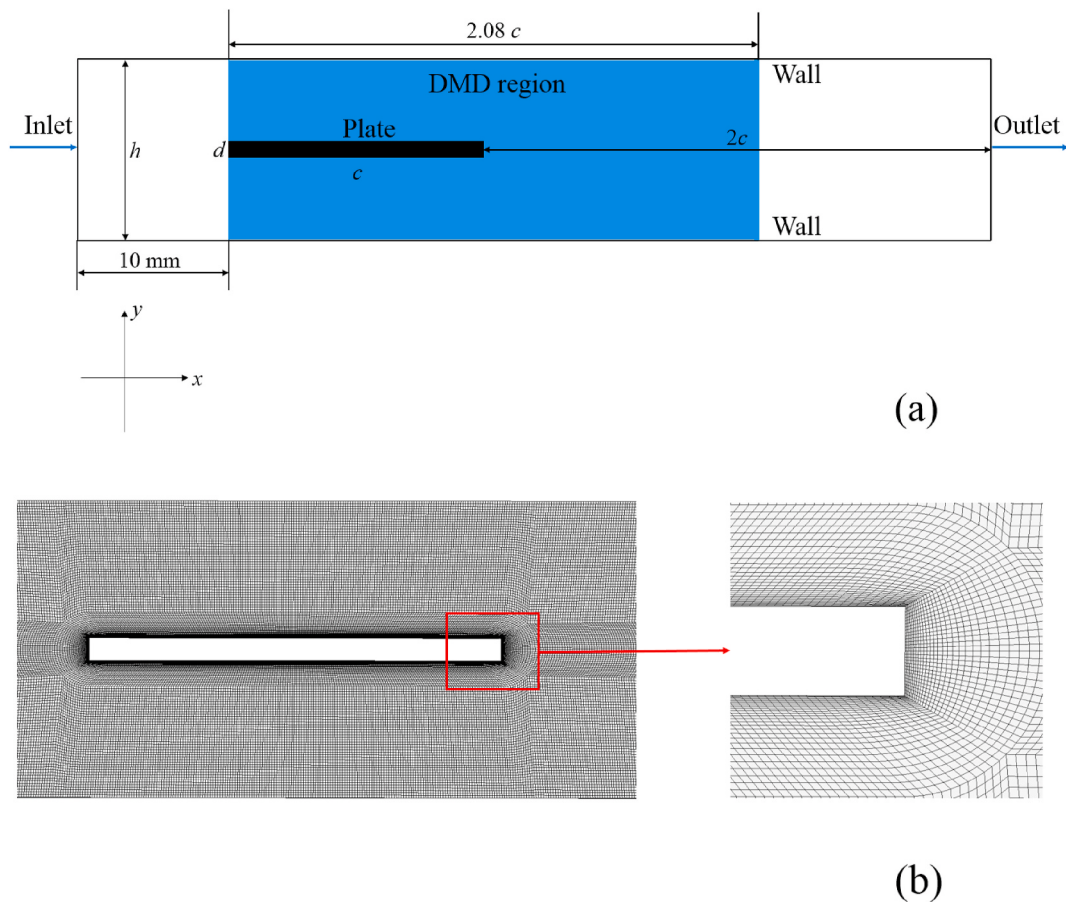


Fig. 2. Configuration for the CFD analysis: (a) computational domain and (b) mesh generation.

profiles obtained from the PIV measurements were applied at the inlet. A spectral synthesizer was employed to simulate the perturbations at the inlet. The “Pressure Outlet” condition was used at the outlet, with the pressure set to 0 Pa. For the wall and plate, the no-slip boundary condition was employed. For the numerical solution, the semi-implicit method for pressure linked equations (SIMPLE) algorithm was used. The second-order implicit scheme for temporal discretization, the least squares cell-based scheme for gradients, and second-order scheme for pressure were used. For momentum, a bounded central differencing scheme was used. The convergence criteria were set to 1×10^{-3} and 1×10^{-6} for continuity and momentum, respectively, while the time step size was set to 10^{-5} s. To study the flow patterns in these cases, the DMD method proposed by Schmid (2010) was employed to decompose the velocity fields. After the calculations reached a steady state, the code was run for an additional 100,000 time steps, and the results were saved after every 10 time steps for the DMD analysis. Thus, the sampling frequency of the DMD was 10 kHz, which was the same as that in the vibration experiments. The DMD region is shown in Fig. 2(a).

3. Results and discussion

3.1. Experimental results

The upstream velocity located 10 mm from the leading edge of the plate was measured by PIV, and the non-dimensional time-averaged velocity profile along the y -direction is shown in Fig. 3. The velocity distribution was reasonable when compared with other experimental results on rectangular channels (Gessner and Emery, 1981; Kaller et al., 2019). In Fig. 3, the velocity profile is mostly flat in the center region of the channel, and the dimensionless velocity on the centerline (U_c/U_b) is

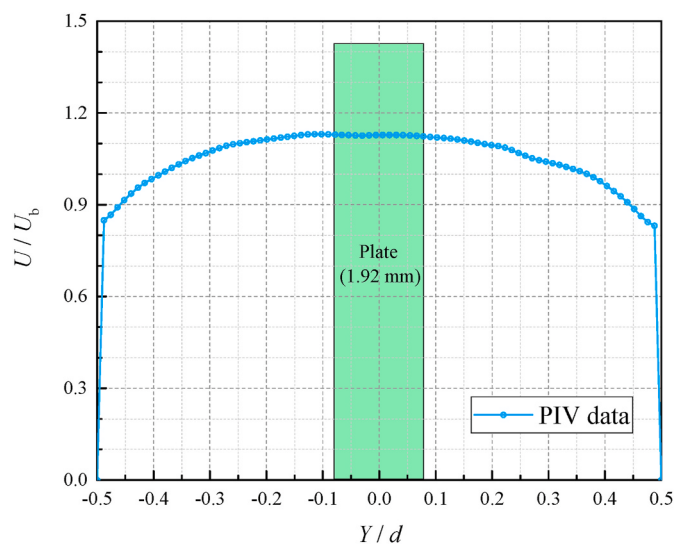


Fig. 3. Time-averaged upstream velocity profile, measured by PIV system on the mid-plane.

1.12. The thickest plate is also shown in Fig. 3, and it was found that the flow velocity around the plate was close to U_c . The most commonly used dimensionless number used for vortex shedding problems is the Strouhal number, which is defined as

$$St = \frac{f_v \cdot \text{characteristic length}}{\text{characteristic velocity}} \quad (10)$$

where f_v is the vortex shedding frequency. In general, the upstream velocity is the characteristic velocity. Considering the results from the PIV measurements, U_c was chosen as the characteristic velocity in the present study. Therefore,

$$St = \frac{f_v \cdot \text{characteristic length}}{U_c} \quad (11)$$

and the characteristic length will be discussed later.

The experimental vibration velocity spectra for Cases 1–5 are shown in Fig. 4. As the upstream flow was turbulent, peaks representing the natural frequencies ($f_{n1}, f_{n2}, f_{n3}, \dots$) also appeared in addition to the peaks induced by vortex shedding (f_v). For Cases 2 and 3, vortex-induced resonance occurred when the vortex shedding frequency was close to the natural frequency of the plate. With an increase in the plate thickness, the vortex shedding frequency decreased. To understand the exact physical mechanism of such flow-induced vibrations, detailed flow structures are needed, which will be discussed in the next section.

3.2. Time-averaged results from numerical simulations

First, the time-averaged results obtained from the numerical simulations described in Section 2.2 will be discussed. Fig. 5 shows the time-averaged pressure contours, where the values for each case were normalized to $[-1, 0]$ for comparison. Case 1 shows different characteristics from those of other cases for pressure around the leading edge. For Case 1, the lowest pressure region was at the leading edge, and the pressure gradually increased with an increase in the distance from the leading edge. For the other five cases, a clearly evident low-pressure region emerged downstream of the leading edge. Additionally, the center of the low-pressure region gradually moved forward to the leading edge of the plate for Cases 2–5. On the other hand, a low-pressure region appeared at the trailing edge for all the cases. Because an adverse pressure gradient would cause flow separation, vortex shedding occurred at both the leading and trailing edges for all the six cases. Comparing Cases 1 and 6, which had the same c/d and h/d , it was

found that the time-averaged pressure distribution was affected by Re_d . On the other hand, Cases 1–5 showed that the sidewall also affected the time-averaged pressure distribution. Moreover, a low-pressure band between the leading and trailing edges was observed for all the cases except Case 1. As Case 1 yielded significantly different behavior compared to the other five cases, it also exhibited a different vortex shedding pattern.

In flows around a flat plate with a square leading edge and high chord-to-thickness ratio, an important phenomenon occurs, whereby separation bubbles get generated at the leading edge, which get reattached to the plate surface downstream. Cherry et al. (1984) summarized that the time-averaged reattachment length of the separation bubble varied from $4.0d$ to $5.5d$. Numerical simulations conducted by Tenaud et al. (2016) yielded a value of $3.68d$ for $Re_d = 7500$, while Tafti and Vanka (1991) obtained $6.36d$ for $Re_d = 1000$. In summary, the reattachment lengths were dispersed and lacked commonality. To investigate the properties of the separation bubble for different cases in this study, time-averaged streamlines are shown in Fig. 6, and the dimensions of the separation bubble are summarized in Table 2. The separation bubbles showed distinct differences, as shown in Fig. 6, where there was only one recirculation region within the separation bubble for Case 1, while this number was two for Cases 2 and 6, and three for Cases 3, 4, and 5. According to the number of recirculation regions, the cases studied in the present study were divided into three types: Type I (one recirculation region), Type II (two recirculation regions), and Type III (three recirculation regions).

The height of the separation bubble (H) and reattachment length (L) are listed in Table 2. For Cases 1–5, the absolute values of H and L increased with an increase in the plate thickness. A quantitative analysis indicated that the aforementioned three types of separation bubbles were reasonable. For Type I, the dimensionless reattachment length was the largest ($L/d = 10$) among all the six cases. Through a combined analysis of the separation bubbles and pressure fields shown in Fig. 5, it can be inferred that the vortices shed from the leading edge of Type I were significantly weak because a low-pressure region was missing in the separation bubble. In addition, the vortex shedding from the leading

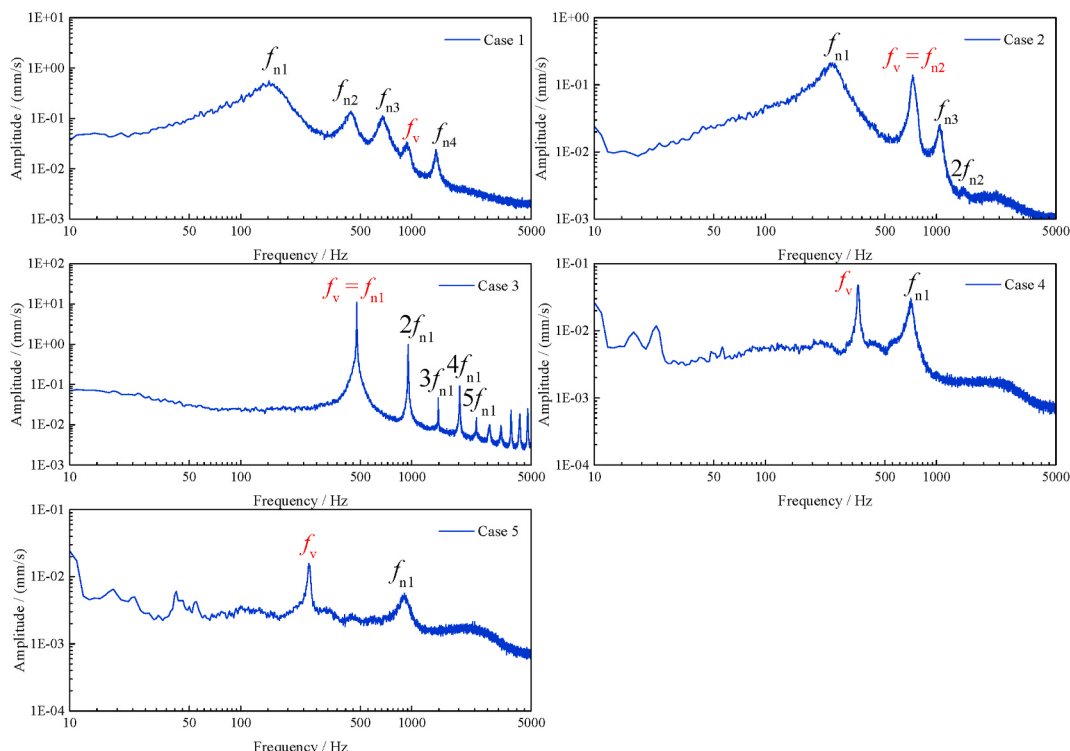


Fig. 4. Experimental velocity spectra for different cases; peaks represent natural and vortex shedding frequencies, and strong resonance occurred for Cases 2 and 3.

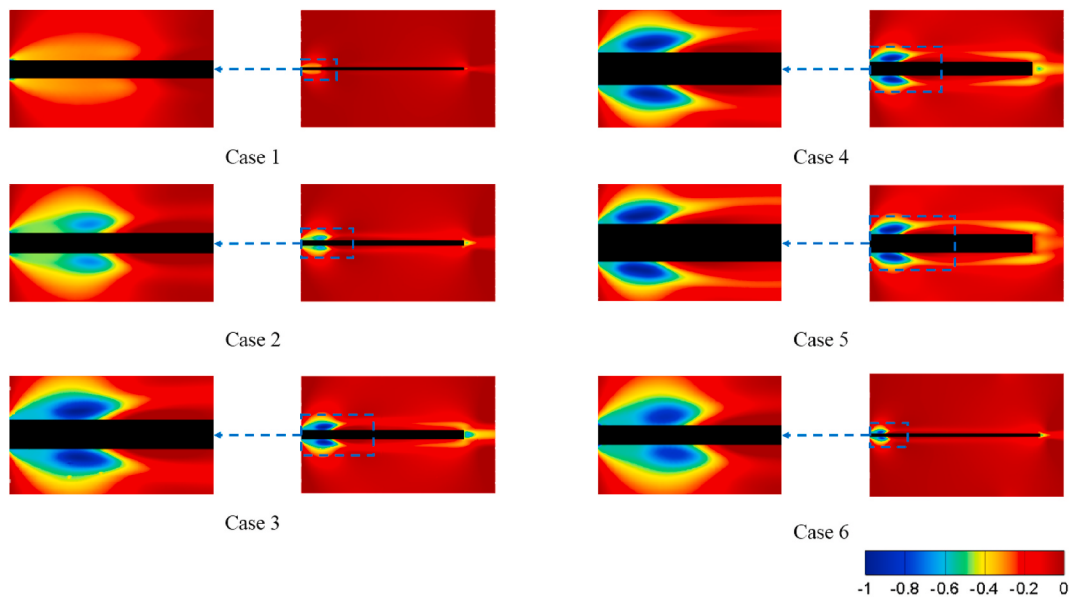


Fig. 5. Time-averaged pressure contours for different cases; low pressure regions emerge at the trailing edge and a low-pressure band between the leading and trailing edges appeared for all the cases except Case 1.

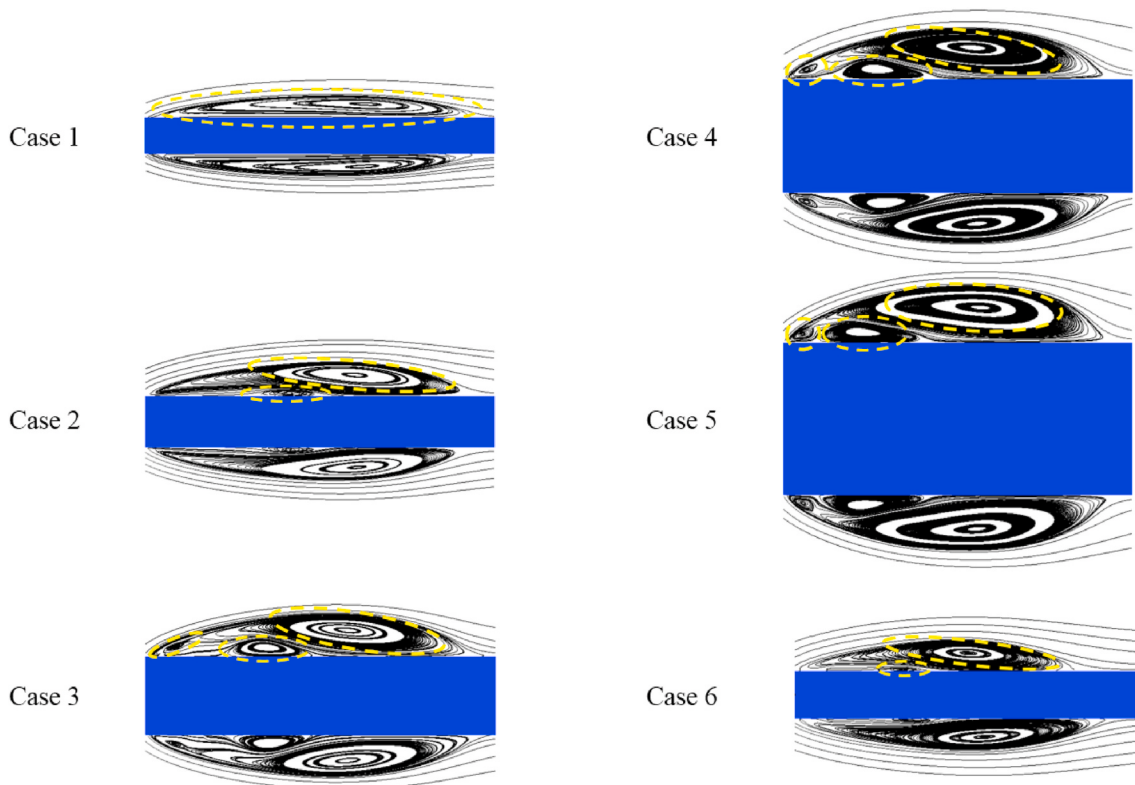


Fig. 6. Time-averaged streamlines at the leading edge for different cases; the dashed lines highlight the recirculation regions.

edge had no effect on the vortices generated at the trailing edge for Type I, as there was no low-pressure band between the leading and trailing edges (Fig. 5). For Type II, the dimensionless values were similar: $H/d = 0.65$ (Case 2) and 0.68 (Case 6), and $L/d = 6.73$ (Case 2) and 6.77 (Case 6). The reattachment length was close to that from the three-dimensional simulation carried out by [Tafti and Vanka \(1991\)](#). Moreover, their study showed that there were two recirculation regions within the separation bubble. However, in the case of Type III, the absolute values of the reattachment length were similar: 4.2, 4.3, and 4.4

mm for Cases 3, 4, and 5, respectively. The values of H/d and L/d decreased with an increase in the plate thickness, or in other words, the decrease in the distance from the plate to the wall. Thus, after the flow condition turning into Type III, the reattachment point was a fixed value from the present data although c/d decreased from 18.3 to 8.8 and h/d decreased from 13.0 to 6.3.

Because the values of c/d and h/d were equal for Cases 1 and 6, the effect of plate thickness or Re_d could be evaluated. From the results shown in Fig. 6 and Table 2, it is clear that Re_d affected the form of the

Table 2

Properties of separation bubbles for different cases; the number of recirculation regions varied with different cases.

Sketch					
Case ID	H/mm	L/mm	H/d	L/d	No. of recirculation regions
Case 1	0.19	3.0	0.62	10.00	1
Case 2	0.34	3.5	0.65	6.73	2
Case 3	0.52	4.2	0.57	4.57	3
Case 4	0.63	4.3	0.45	3.09	3
Case 5	0.72	4.4	0.38	2.29	3
Case 6	1.30	13.0	0.68	6.77	2

separation bubble. With an increase in Re_d from 597 to 3822, a new recirculation region developed within the separation bubble. Moreover, Cases 2 and 6 were similar in terms of the recirculation type and dimensionless lengths of the separation bubble. Therefore, the transition of the separation bubble from Type I to Type II occurred when Re_d reached 1035. For Cases 1, 2, and 6, the problem could be treated as a flow around a long flat plate in a large domain because the dimensionless heights of the separation bubbles of the three cases were relatively large and close to one another. Comparing Cases 5 and 6, the sidewall affected the characteristics of the separation bubbles as one more recirculation region developed and the dimensionless lengths of the separation bubbles decreased. Therefore, when the distance from the plate to the sidewall decreased, the form of the separation bubble changed to that of Type III. Moreover, the dimensionless height and length decreased with a decrease in h/d , which meant that the separation bubble was compressed when the plate was close to the sidewall.

The time-averaged results obtained through numerical simulations showed that both h/d and Re_d affected the flow fields around the plate with a high c/d . Two types of pressure distribution (existence of low pressure band) and three types of separation bubbles (number of recirculation regions within it) were observed. These results revealed that the

vortex shedding for different cases obeyed different rules; therefore, the unsteady results will be discussed later.

3.3. Unsteady-state results from numerical simulations

To thoroughly study the vortex shedding patterns and characteristics of the plates employed in the present study, unsteady-state results were extracted from the numerical simulations. Moreover, because the frequency of vortex-induced vibration is the only parameter that could illustrate the unsteady characteristics from the experiments, it was necessary to acquire the corresponding results from the simulations to validate the current numerical method.

The instantaneous vorticity contours for different simulations are shown in Fig. 7. From the results, as mentioned before, it can be observed that vortices were shed from both the leading and trailing edges. However, the detailed unsteady characteristics were different, corresponding to the three recirculation types mentioned above. For Type I, the vortices shed from the leading edge did not move far away from the surface of the plate when transported to the trailing edge. These leading edge vortices were adjacent to the boundary layer and diffused before reaching the trailing edge. From the leading edge, only a single vortex was shed with either positive or negative vorticity. For Type II, the leading edge vortices still survived when they reached the trailing edge. In addition, the leading edge vortices contacted the trailing-edge vortices. Another important phenomenon was that the vortex shedding from the leading edge was accompanied by a small vortex, which had an opposite direction of vorticity. These vortex pairs are highlighted by a dashed line, in Fig. 7. From the separation bubble analysis, presented in Section 3.2, it can be observed that the larger vortex pair corresponded to the larger recirculation region, while the smaller one corresponded to the smaller recirculation region beneath the larger one within the separation bubble. However, the smaller vortex was quite weak and diffused before reaching the trailing edge. Type III was quite similar to Type II, and the leading edge vortices were vortex pairs, as there were three recirculation regions within the separation bubble. The

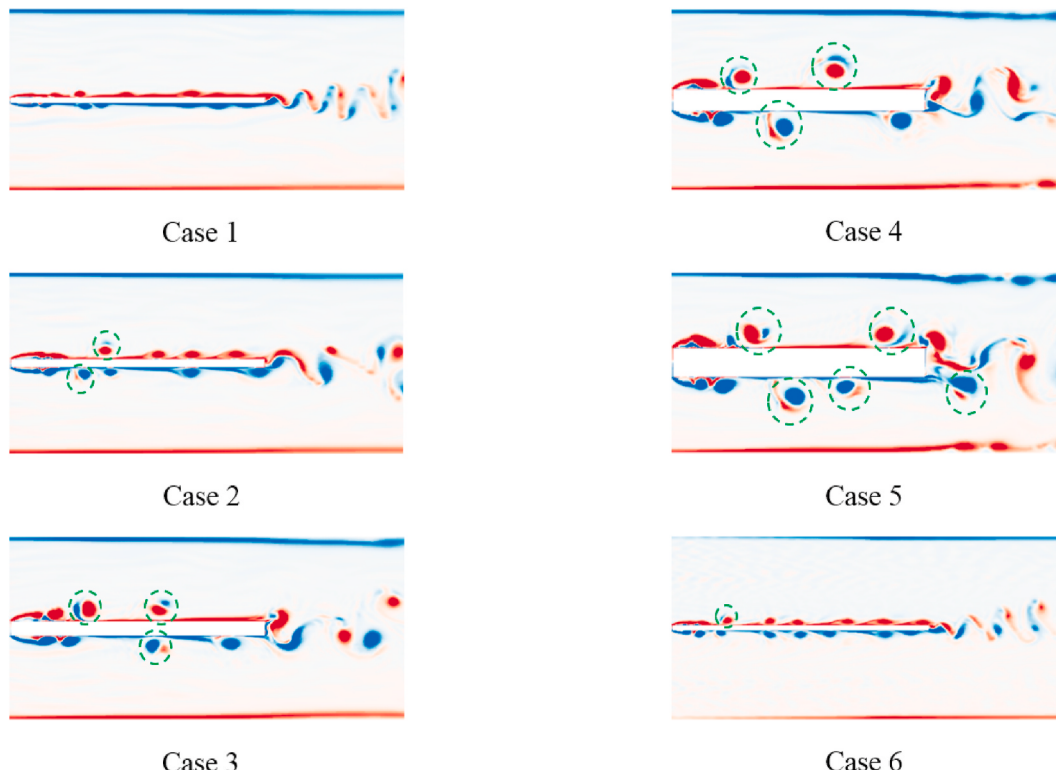


Fig. 7. Instantaneous contours of vorticity for different cases; the dashed lines highlight the vortex pairs.

difference between Types II and III is that the smaller of the vortex pair still survived when it reached the trailing edge. These results are reasonable because the recirculation region, which corresponded to the smaller vortex, was larger than that in Type II. Comparing the instantaneous vorticity contours of Types I, II, and III, the existence of an opposite vortex caused the vortex pairs to depart from the plate surface. For Type III, there was a specific distance from the vortex pairs to the plate surface. A more conspicuous phenomenon that illustrates the influence of the opposite vortex developed in Type II, i.e., there was a distance between the vortex pairs near the leading edge and the plate surface; however, the vortex was “captured” by the boundary layer after the opposite vortex diffused. Therefore, the opposite vortex pushed the accompanying vortex away from the plate and prevented the merging of the boundary layer and the vortices.

From the pressure distribution shown in Fig. 5, streamlines in Fig. 6, and vorticity contours in Fig. 7, we can draw some preliminary conclusions. When the freestream impacted the long flat plate under a low Re_d condition (in a large domain), a low-pressure region formed at the leading edge, and vortex shedding happened owing to the adverse pressure gradient. As the pressure gradient was quite small (Fig. 5), the leading edge vortices got detached at a position far away from the leading edge (dimensionless length). These vortices were significantly weak and could not induce fluid entrainment into the separation zone. In addition, the leading edge vortices diffused before reaching the trailing edge in the present study ($Re_d = 597$ and $c/d = 56.0$). Then, increasing the Re_d and maintaining the large-space condition generated a low-pressure core downstream of the leading edge. The low-pressure core had a larger differential pressure than the previous case and hence, stronger leading edge vortices were generated. These vortices induced the entrainment of fluid into the separation bubble, which in turn, generated vortices in the opposite direction. Then, the two vortices became coupled as a vortex pair and departed from the plate in the transverse direction. The opposite vortex diffused later, and the remaining vortex was connected to the boundary layer. Then, the leading edge vortices reached the trailing edge and were shed with the vortices formed there. After introducing the effect of the sidewalls, the

differential pressure of the low-pressure region at the leading edge increased. Under these conditions, the vortices generated owing to the entrainment of fluid were strong enough to cause a secondary entrainment, which resulted in the third recirculation region near the leading edge, as shown in Fig. 6. These vortex pairs survived until they reached the trailing edge.

To directly discern the shedding mode, the DMD was applied to decompose the velocity fields, extracted from the simulation results. The spectra of all the cases investigated are shown in Fig. 8, where the ordinate represents the energy (L_2 -norm) of the DMD modes. The highest energy mode is indicated by its frequency. The main goal of the simulation was to determine the shedding frequency and the corresponding mode. In the present study, the highest energy modes were the main vortex shedding patterns, and their frequencies were regarded as the vortex-induced vibration frequencies. The experimental and numerical shedding frequencies are shown in Table 3, which are in good agreement with each other, thus validating the numerical model presented in Section 2.2.

The DMD modes of maximal energy for each case are shown in Fig. 9, and the distributions of transverse velocity were demonstrated here because the values are the typical parameters for vortex shedding. For each case, the results were renormalized in the interval $[-1, 1]$. From the contours shown in Fig. 9, it is clear that there were different vortex shedding modes among the six cases. For Case 1 (Type I), weak vortices were generated at the leading edge, which diffused before reaching the trailing edge. The vortices formed at the trailing edge constituted a

Table 3
Comparison between experimental and numerical results.

Case ID	Experimental/Hz	Numerical/Hz	Deviation/%
Case 1	931	923.0	0.86
Case 2	726	689.7	5.00
Case 3	477	462.1	3.12
Case 4	348	340.0	2.30
Case 5	250	258.6	3.44

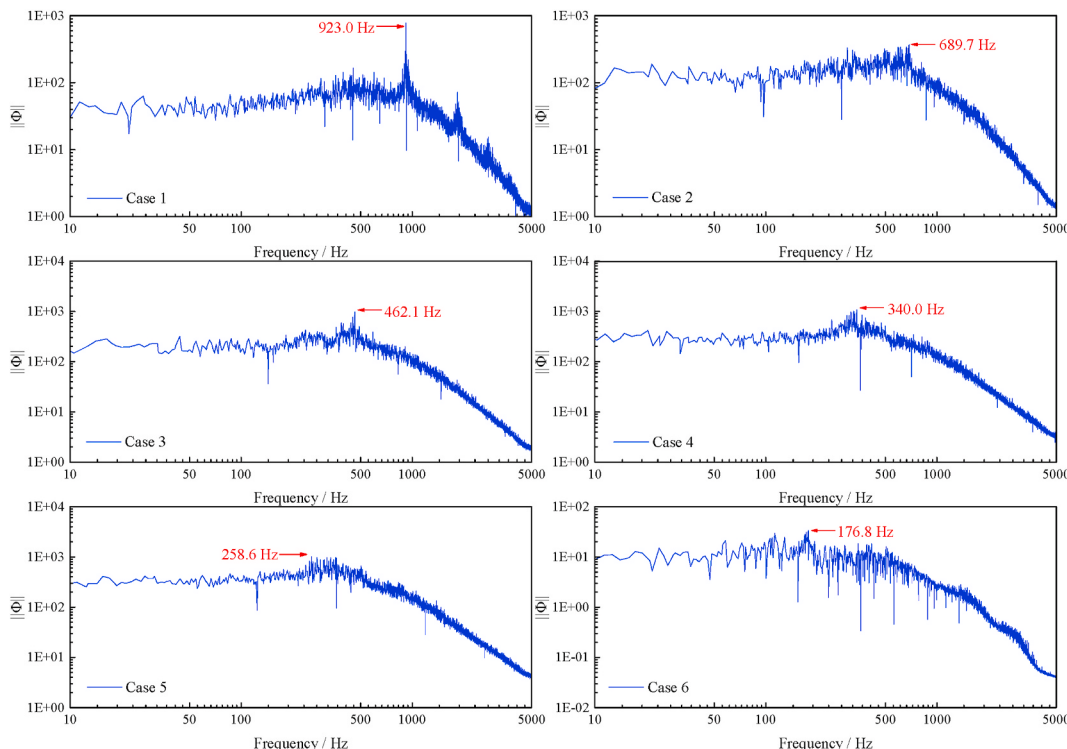


Fig. 8. DMD spectra for different cases; the frequencies of modes with the highest energy are indicated by red arrows.

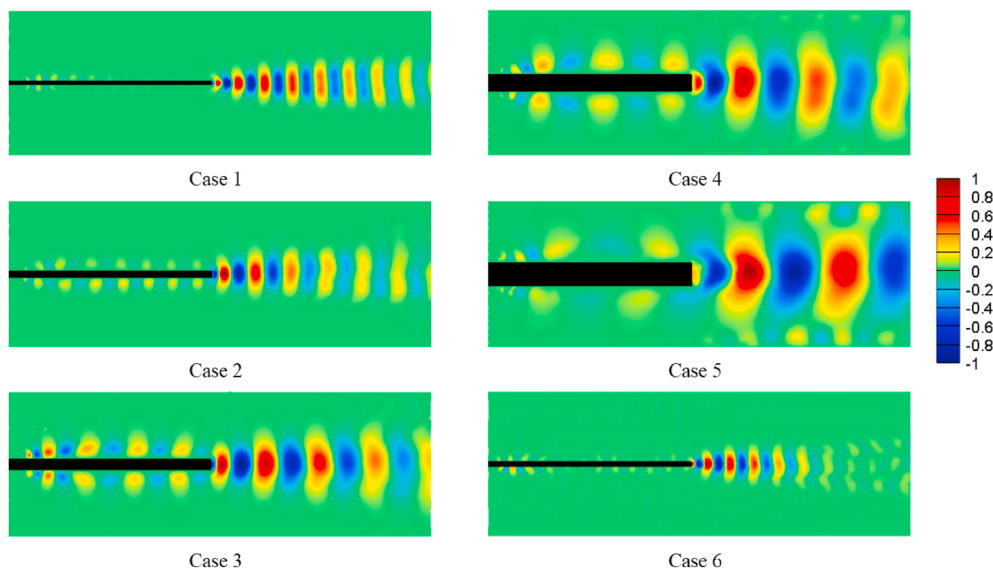


Fig. 9. Normalized DMD modes (transverse velocity) of maximum energy for each case.

regular vortex street downstream. Therefore, the shedding pattern for Type I was trailing edge shedding. For Cases 2 and 6 (Type II), compared with the trailing-edge vortices, the vortices detached from the leading edge were also weak. However, these leading-edge vortices sustained and were transported to the trailing edge, which was the same as previously mentioned. The leading edge vortices were close to the plate surface during their movement from the leading edge to the trailing edge. Moreover, compared with Type I, the downstream vortices of Type II decayed more quickly. Finally, the leading and trailing edge vortices showed strong coupling effect in Case 3, 4, and 5 (Type III). It is evident that the transverse velocity patches downstream of the trailing edge showed irregular shapes for Type III, while they were nearly elliptical for Types I and II. From the DMD modes of the three cases, it can be observed that the vortices were first generated near the leading edge, which then departed from the plate surface in the transverse direction, and moved close to the plate surface again. This departure behavior was induced by vortex pairs, as discussed previously. These leading-edge vortices finally contacted the vortices growing at the trailing edge and were shed together. During the process, the leading edge vortices were conveyed to the trailing edge, and their intensities gradually decayed. Moreover, with regard to the tailing edge vorticity, Case 3 showed the highest relative intensity of the leading edge, while Case 5 showed the lowest. In addition, vortex shedding from the trailing edge in Case 5 was of high intensity because the vortices at the sidewalls were induced by the shedding process.

From the DMD modes (Fig. 9) and the time-averaged pressure distributions (Fig. 5), the low-pressure band, which linked the leading and trailing edges as shown in Fig. 5, indicates the route of the leading-edge vortices. For Type I, the vortices were generated in the low-pressure region and diffused quickly; thus, no distinct low-pressure band was developed. For Type II, the low-pressure band was close to the plate surface because the leading-edge vortices were also close to the plate. For Type III, the low-pressure band first departed from the plate surface in the transverse direction and then moved back again. Therefore, it was clear that three vortex shedding modes existed among the six numerical simulations, namely trailing-edge shedding without leading edge–vortices coupling (Type I), weak leading edge–vortices coupled shedding (Type II), and strong leading edge–vortices coupled shedding (Type III).

3.4. Discussion on strouhal number

Based on Eq. (11), the St_d values were calculated to be 0.124, 0.160, 0.190, 0.211, 0.222, and 0.152 for the six cases, respectively. The obvious differences in the calculated St_d values were owing to the three different vortex shedding modes discussed above. Therefore, an effort was made to find a robust Strouhal number, considering the three shedding modes for a single elongated plate.

The proposed method uses the separation distance between similarly shed rotational vortices (λ) obtained from the DMD analysis as the characteristic length. The calculated separation distances are shown in Fig. 10, where “Sequence” represents the sequence of the appearance of λ at the downstream of the trailing edge. It was found that for all the cases, λ first increased with the vortices departing from the trailing edge, and then reached a stable value. Note that for Case 5, the stable value was acquired through extrapolation because λ in its DMD region did not converge. The stable λ was used as the characteristic length to calculate St_d .

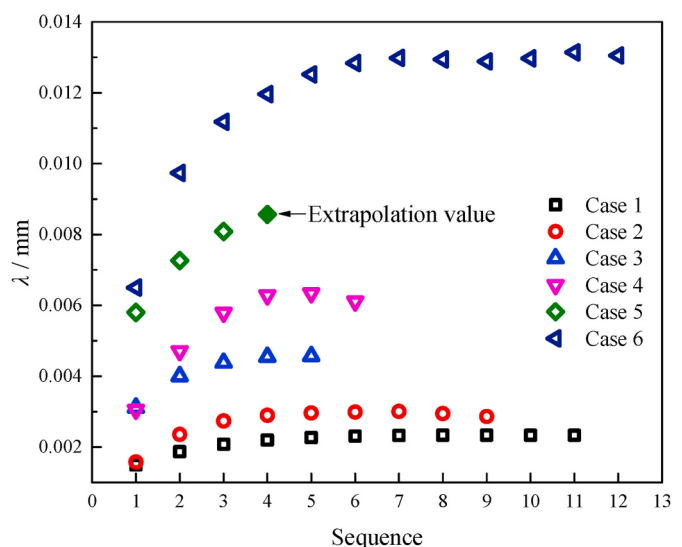


Fig. 10. Variation of separation distances between similarly shed rotational vortices downstream of the trailing edge. For Case 5, the last value was obtained through extrapolation.

Another choice was the thickness of the boundary layer at the trailing edge. The definition of the boundary layer could be adopted directly for the flow around a structure in an open space. However, both the side-walls and a pressure gradient were present in the current study. Therefore, the “boundary layer” needed to be modified. Here, we also employed the thickness of the plate as part of the characteristic length, and the time-averaged distributions of the flow velocity along the dimensionless transverse direction (Y/d) at the trailing edge are shown in Fig. 11. It can be observed that before the flow velocity reached U_c , the velocity distribution of a higher St_d constituted an envelope for the lower St_d cases. Therefore, we set the distance from the plate surface to the point where $U = U_c$ as the boundary layer thickness δ in the present study.

The boundary layer thicknesses are summarized in Table 4. From the results, it can be observed that the scaled thickness δ/d decreased with an increase in St_d . Moreover, increasing the intensity of the leading edge vortices could result in a decrease in δ/d . Thus, the consequence of the leading edge vortices participating in the overall vortex shedding was that the vortices developing from the leading edge made the boundary layer at the trailing edge thinner (compared with the case of no leading edge vortices) and accelerated the vortex shedding. This acceleration was related to the intensity of the leading edge vortices; as stronger vortices would lead to a higher frequency. In addition, as both d and δ were used here, the final form of the characteristic length was $d+2\delta$, and the corresponding Strouhal number was $St_{t+2\delta}$.

The results of the Strouhal numbers in different forms are summarized in Table 5. Both $St_{d+2\delta}$ and St_λ showed better universality than St_d . The relative standard deviations (RSDs) of $St_{d+2\delta}$ and St_λ were 5.4% and 3.5%, respectively, which were much smaller than that of St_d , which was of 21.3%. Therefore, the thickness of the plate with a boundary layer thickness of $d + 2\delta$ or the separation distance between similarly shed rotational vortices λ were more appropriate characteristic lengths to describe the vortex shedding behavior in the present study for the elongated flat plate with square leading and trailing edges in a confined rectangular channel.

4. Conclusions

Both experimental and numerical investigations were carried out to study the vortex shedding characteristics of a single flat plate with a high chord-to-thickness ratio and rectangular cross-section in a confined rectangular channel. The flow-induced vibration of the plate was

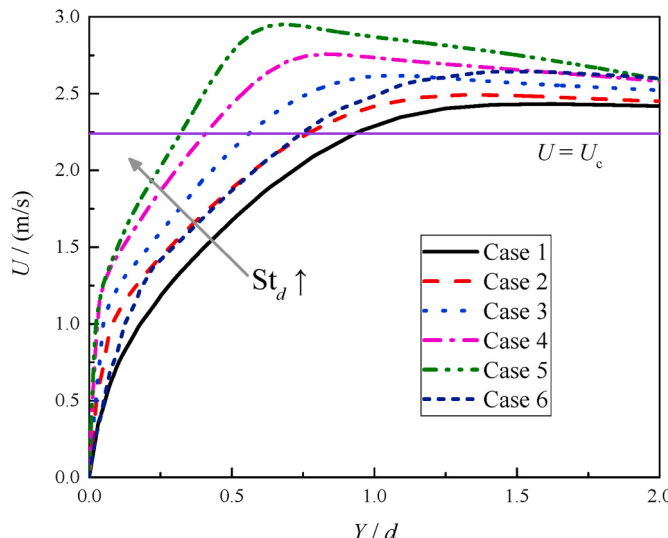


Fig. 11. Time-averaged flow velocity (x -direction) distribution along the dimensionless transverse direction (y -direction) at the trailing edge for different cases.

Table 4

Boundary layer thicknesses for different cases; the scaled thickness δ/d decreased with increasing St_d .

Case ID	δ/mm	δ/d	St_d
Case 1	0.28	0.93	0.124
Case 2	0.40	0.77	0.160
Case 3	0.52	0.56	0.190
Case 4	0.57	0.41	0.211
Case 5	0.62	0.32	0.222
Case 6	1.43	0.74	0.152

Table 5

Summary of results for different Strouhal numbers. $St_{d+2\delta}$ and St_λ showed more robustness than St_d .

Case ID	St_d	$St_{d+2\delta}$	St_λ
Case 1	0.124	0.355	0.960
Case 2	0.160	0.406	0.924
Case 3	0.190	0.403	0.939
Case 4	0.211	0.383	0.956
Case 5	0.222	0.364	0.989
Case 6	0.152	0.377	1.016
RSD	21.3%	5.4%	3.5%

measured by LDV and the corresponding characteristic vibration frequency reflected the vortex shedding phenomenon around the plate. In addition, the flow velocity distribution upstream of the plate was acquired by PIV measurements, and the results were set as the inlet boundary conditions for subsequent numerical simulations. The LES together with the WALE model was adopted to simulate the detailed flow structure around the plate, and the DMD was employed to extract the vortex shedding information. A total of 5 sets of experimental measurements and six simulations of numerical cases with different c/d and h/d were investigated considering the same upstream velocity profile. The predicted vortex shedding frequencies matched well with the experimental characteristic vibration frequencies, measured by LDV.

From the numerical results, three vortex shedding modes were found, namely trailing edge shedding without the leading edge–vortices coupling (Type I), weak leading edge–vortices coupled shedding (Type II), and strong leading edge–vortices coupled shedding (Type III). For Type I, the vortices generated at the leading edge could hardly reach the trailing edge, and the vortex shedding was dominated by the trailing edge. For Type II, the leading edge vortices could survive until they reached the trailing edge and induced trailing edge shedding. These leading edge vortices were strong enough to induce entrainment of fluid into the separation bubble and generate small vortices with an opposite direction of vorticity. On the other hand, the leading-edge vortices were also weak enough so that the opposite vortices quickly diffused and could not exert an obvious effect. For Type III, the intensity of the leading edge vortices increased adequately so that the opposite vortices could maintain and cause the large vortices to depart from the plate surface. In addition, the vortex pairs approached the trailing edge and were shed along with the trailing edge vortices. Owing to the three different shedding modes, the time-averaged results of the flow fields were also altered. Low-pressure regions developed at both the leading and trailing edges in all the cases. However, there was no low-pressure core downstream of the leading edge, and the low-pressure band connecting the leading and trailing edges was also missing for Type I. For Types II and III, there was a distinct low-pressure core at the downstream of the leading edge. The low-pressure band was close to the plate surface for Type II, while it first departed and then moved back to the plate surface in the transverse direction for Type III. In addition, the recirculation regions within the separation bubble were also different — one for Type I, two for Type II, and three for Type III. The Reynolds number based on the plate thickness Re_d and the distance from the sidewall to the plate could alter the vortex shedding mode.

To establish a robust Strouhal number for the present problem, the boundary layer thickness at the trailing edge and separation distances between similarly shed rotational vortices downstream of the plate were analyzed. The results showed that $St_{d+2\delta}$ and St_λ were more robust than St_d . Moreover, the leading edge vortices could make the boundary layer thickness at the trailing edge thinner, and this effect was strengthened with an increase in the intensity of the leading edge vortices. These results could be considered as representative behavior of vortex shedding of real spacer grids and as a foundation for further investigations on flow-induced vibrations of spacer grids.

Declaration of competing interest

The authors declare that they have no known competing financial interests or personal relationships that could have appeared to influence the work reported in this paper.

Acknowledgments

This work was supported by the Sichuan Province Science Funds for Distinguished Young Scholars (No. 2020JDJQ0069).

References

- Cherry, N.J., Hillier, R., Latour, M.E.M.P., 1984. Unsteady measurements in a separated and reattaching flow. *J. Fluid Mech.* 144, 13–46.
- De Santis, D., Kottapalli, S., Shams, A., 2018. Numerical simulations of rod assembly vibration induced by turbulent axial flows. *Nucl. Eng. Des.* 335, 94–105.
- Gessner, F.B., Emery, A.F., 1981. The numerical prediction of developing turbulent flow in rectangular ducts. *J. Fluid Eng.* 103, 445–453.
- Houigan, K., Thompson, M.C., Tan, B.T., 2001. SELF-SUSTAINED oscillations IN flows around long blunt plates. *J. Fluid Struct.* 15, 387–398.
- Jiang, H., Qu, J., Lu, R.Y., Wang, J.-A.J., 2016. Grid-to-rod flow-induced impact study for PWR fuel in reactor. *Prog. Nucl. Energy* 91, 355–361.
- Kaller, T., Pasquariello, V., Hickel, S., Adams, N.A., 2019. Turbulent flow through a high aspect ratio cooling duct with asymmetric wall heating. *J. Fluid Mech.* 860, 258–299.
- Kaneko, S., Nakamura, T., Inada, F., Kato, M., Ishihara, K., Nishihara, T., Langthjem, M. A., 2014. Flow-induced Vibrations, second ed. Academic Press, Oxford.
- Kim, K.-T., 2009. The study on grid-to-rod fretting wear models for PWR fuel. *Nucl. Eng. Des.* 239, 2820–2824.
- Kou, J., Le Clainche, S., Zhang, W., 2018. A reduced-order model for compressible flows with buffeting condition using higher order dynamic mode decomposition with a mode selection criterion. *Phys. Fluids* 30, 016103.
- Liu, Y., Zhang, Q., 2015. Dynamic mode decomposition of separated flow over a finite blunt plate: time-resolved particle image velocimetry measurements. *Exp. Fluid* 56, 148.
- Mills, R., Sheridan, J., Hourigan, K., 2002. Response of base suction and vortex shedding from rectangular prisms to transverse forcing. *J. Fluid Mech.* 461, 25–49.
- Mondal, R., Alam, M.M., Bhatt, R., 2020. Effect of side walls on flow around prisms. *Ocean Eng.* 196, 106797.
- Naghib-Lahouti, A., Lavoie, P., Hangan, H., 2014. Wake instabilities of a blunt trailing edge profiled body at intermediate Reynolds numbers. *Exp. Fluid* 55, 1779.
- Nakamura, Y., Ohya, Y., Tsuruta, H., 1991. Experiments on vortex shedding from flat plates with square leading and trailing edges. *J. Fluid Mech.* 222, 437–447.
- Naudascher, E., Wang, Y., 1993. Flow-induced vibrations of prismatic bodies and grids of prisms. *J. Fluid Struct.* 7, 341–373.
- Nicoud, F., Ducros, F., 1999. Subgrid-scale stress modelling based on the square of the velocity gradient tensor. *Flow, Turbul. Combust.* 62, 183–200.
- Parker, R., 1966. Resonance effects in wake shedding from parallel plates: some experimental observations. *J. Sound Vib.* 4, 62–72.
- Parker, R., Welsh, M.C., 1983. Effects of sound on flow separation from blunt flat plates. *Int. J. Heat Fluid Flow* 4, 113–127.
- Pettigrew, M.J., Taylor, C.E., Fisher, N.J., Yetisir, M., Smith, B., 1998. Flow-induced vibration: recent findings and open questions. *Nucl. Eng. Des.* 185, 249–276.
- Rojratsirikul, P., Genc, M.S., Wang, Z., Gursul, I., 2011. Flow-induced vibrations of low aspect ratio rectangular membrane wings. *J. Fluid Struct.* 27, 1296–1309.
- Rowley, C.W., Mezić, I., Bagheri, S., Schlatter, P., Henningson, D.S., 2009. Spectral analysis of nonlinear flows. *J. Fluid Mech.* 641, 115–127.
- Schmid, P.J., 2010. Dynamic mode decomposition of numerical and experimental data. *J. Fluid Mech.* 656, 5–28.
- Shi, L.L., Liu, Y.Z., Yu, J., 2010. PIV measurement of separated flow over a blunt plate with different chord-to-thickness ratios. *J. Fluid Struct.* 26, 644–657.
- Shiraishi, N., Matsumoto, M., 1983. On classification of vortex-induced oscillation and its application for bridge structures. *J. Wind Eng. Ind. Aerod.* 14, 419–430.
- Stokes, A.N., Welsh, M.C., 1986. Flow-resonant sound interaction in a duct containing a plate, II: square leading edge. *J. Sound Vib.* 104, 55–73.
- Tafti, D.K., Vanka, S.P., 1991. A numerical study of flow separation and reattachment on a blunt plate. *Phys. Fluid. Fluid Dynam.* 3, 1749–1759.
- Tan, B.T., Thompson, M.C., Hourigan, K., 2004. Flow past rectangular cylinders: receptivity to transverse forcing. *J. Fluid Mech.* 515, 33–62.
- Taylor, Z.J., Palombi, E., Gurka, R., Kopp, G.A., 2011. Features of the turbulent flow around symmetric elongated bluff bodies. *J. Fluid Struct.* 27, 250–265.
- Tenaud, C., Podvin, B., Fraigneau, Y., Daru, V., 2016. On wall pressure fluctuations and their coupling with vortex dynamics in a separated–reattached turbulent flow over a blunt flat plate. *Int. J. Heat Fluid Flow* 61, 730–748.
- Tu, J.H., Rowley, C.W., Luchtenburg, D.M., Brunton, S.L., Kutz, J.N., 2014. On dynamic mode decomposition: theory and applications. *J. Comput. Dynam.* 1, 391–421.
- Weaver, D.S., Ziada, S., Au-Yang, M.K., Chen, S.S., Paidoussis, M.P., Pettigrew, M.J., 2000. Flow-induced vibrations in power and process plant components—progress and prospects. *J. Pressure Vessel Technol.* 122, 339–348.
- Welsh, M.C., Gibson, D.C., 1979. Interaction of induced sound with flow past a square leading edged plate in a duct. *J. Sound Vib.* 67, 501–511.
- Zhang, C., Ding, J., Zheng, Y., Gan, F., Gong, S., Mei, Y., 2017. Crucial factors analysis of 5×5 grid flow-induced vibration test. In: Proceedings of the 25th International Conference on Nuclear Engineering. ICONE25, Shanghai, China. V003T002A031.
- Zhang, Q., Liu, Y., 2015. Influence of incident vortex street on separated flow around a finite blunt plate: PIV measurement and POD analysis. *J. Fluid Struct.* 55, 463–483.